A heterogeneous single-atom palladium catalyst surpassing homogeneous systems for Suzuki coupling

Zupeng Chen[1,5], Evgeniya Vorobyeva[1,5], Sharon Mitchell[1], Edvin Fako[2], Manuel A. Ortuño[2], Núria López[2], Sean M. Collins[3], Paul A. Midgley[3], Sylvia Richard[4], Gianvito Vilé[4] and Javier Pérez-Ramírez[1*]

Palladium-catalysed cross-coupling reactions, central tools in fine-chemical synthesis, predominantly employ soluble metal complexes despite recognized challenges with product purification and catalyst reusability[1–3]. Attempts to tether these homogeneous catalysts on insoluble carriers have been thwarted by suboptimal stability, which leads to a progressively worsening performance due to metal leaching or clustering[4]. The alternative application of supported Pd nanoparticles has faced limitations because of insufficient activity under the mild conditions required to avoid thermal degradation of the substrates or products. Single-atom heterogeneous catalysts lie at the frontier[5–18]. Here, we show that the Pd atoms anchored on exfoliated graphitic carbon nitride (Pd-ECN) capture the advantages of both worlds, as they comprise a solid catalyst that matches the high chemoselectivity and broad functional group tolerance of state-of-the-art homogeneous catalysts for Suzuki couplings, and also demonstrate a robust stability in flow. The adaptive coordination environment within the macroheterocycles of ECN facilitates each catalytic step. The findings illustrate the exciting opportunities presented by nanostructuring single atoms in solid hosts for catalytic processes that remain difficult to heterogenize.

Palladium atoms isolated in graphitic carbon nitride exhibit, at first glance, coordination spheres closely resembling those of typical homogeneous C–C coupling catalysts, which include $Pd(OAc)_2$ (palladium acetate), $Pd(PPh_3)_4$ (tetrakis(triphenylphosphine)palladium) and $Pd(dtbpf)Cl_2$ ([1,1′-bis(di-*tert*-butylphosphino)ferrocene]dichloropalladium(II)), and to palladium acetate anchored on silica functionalized by 3-mercaptopropyl ethyl sulfide (PdAc-MPES/SiO_2), one of the most successful commercial heterogeneous catalysts for Suzuki couplings (Fig. 1). Comparatively, common heterogeneous palladium catalysts based on supported nanoparticles, such as Pd/C or even strongly modified Lindlar-type Pd–Pb/$CaCO_3$, feature very different geometric and electronic properties. Microwave-irradiation-assisted deposition was used to introduce palladium on ECN, a pristine high-surface form of graphitic carbon nitride obtained by thermal exfoliation without alteration of the carrier structure (Supplementary Fig. 1). The sole presence of isolated palladium atoms is confirmed by aberration-corrected scanning transmission electron microscopy (AC-STEM) (Fig. 2a and Supplementary Fig. 2) and extended X-ray absorption fine structure spectroscopy (Fig. 2c). A quantitative analysis of the atom positions in the high-angle annular dark-field images highlights the good match between the measured nearest-neighbour distances and

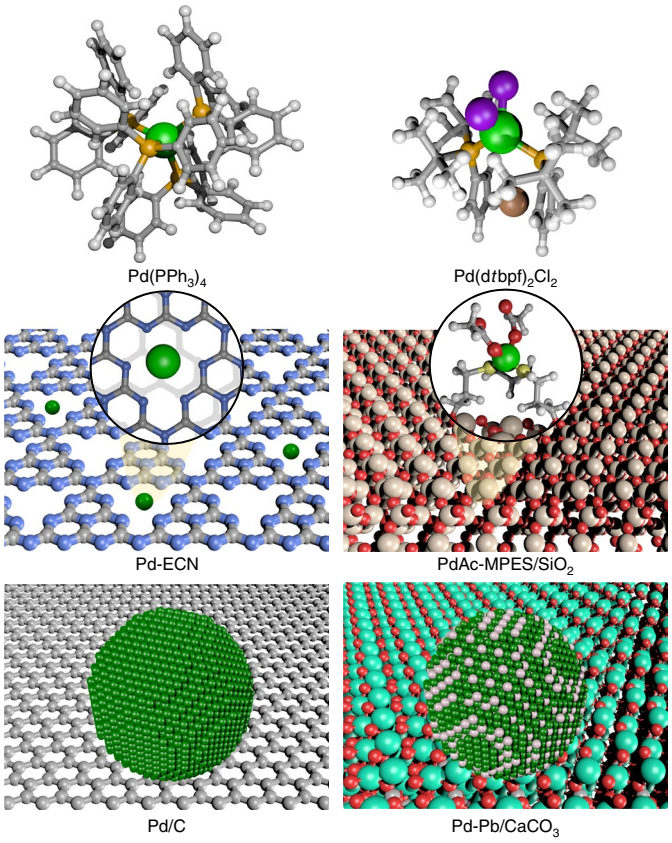

Fig. 1 | Structural comparison of the catalysts. Schematic illustrations of the homogeneous and heterogeneous palladium catalysts studied in the Suzuki reaction.

[1]Institute for Chemical and Bioengineering, Department of Chemistry and Applied Biosciences, ETH Zürich, Zürich, Switzerland. [2]Institute of Chemical Research of Catalonia (ICIQ), The Barcelona Institute of Science and Technology, Tarragona, Spain. [3]Department of Materials Science and Metallurgy, University of Cambridge, Cambridge, UK. [4]Chemistry Technologies and Lead Discovery, Department of Drug Discovery and Clinical Development, Idorsia Pharmaceuticals Ltd, Allschwil, Switzerland. [5]These authors contributed equally: Zupeng Chen, Evgeniya Vorobyeva. *e-mail: jpr@chem.ethz.ch

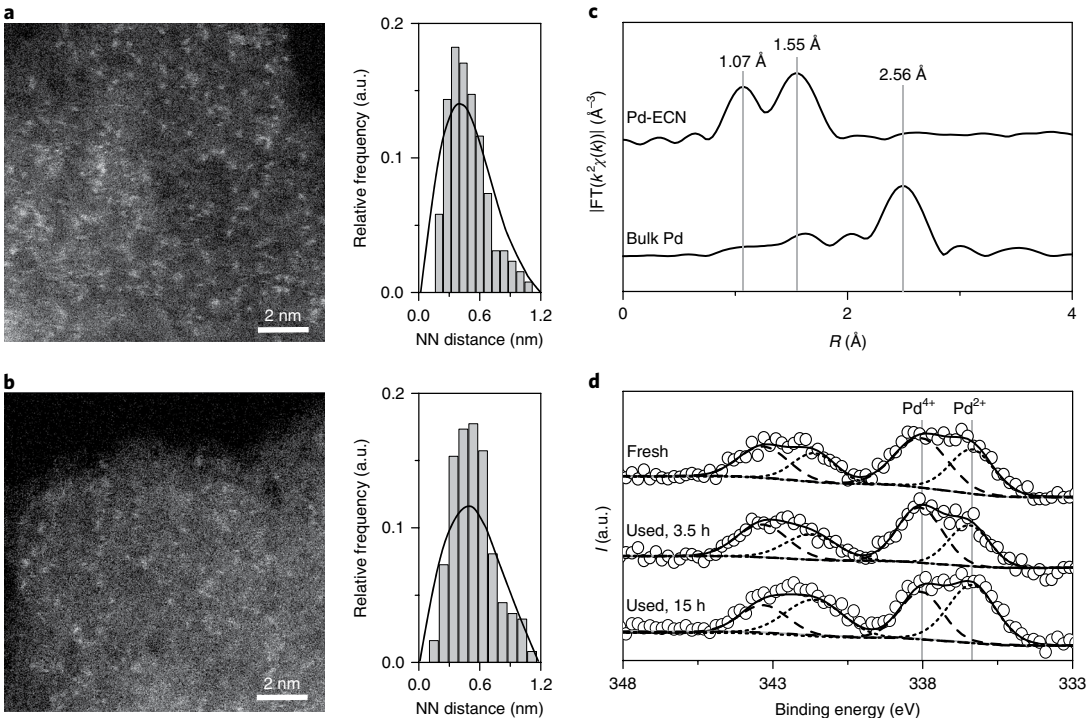

Fig. 2 | Properties of Pd-ECN. a,**b**, AC-STEM images of the fresh (**a**) and used (for 15 h) (**b**) Pd-ECN catalyst, and the corresponding nearest-neighbour (NN) distances of the Pd atoms. The black lines indicate the Rayleigh distribution expected for a random distribution of points in the same area, and confirm the single-atom nature of Pd-ECN. **c**, Normalized magnitudes of the k^2-weighted Fourier transform (FT) of the extended X-ray absorption fine structure spectra in radial distance (R). **d**, Pd 3d core level XPS spectra of the catalyst in fresh and used form. In **d**, the solid black lines show the fitted result of the raw data (open circles), whereas the dashed and dotted black lines correspond to the deconvoluted components. The grey lines indicate the position of the assigned Pd^{4+} and Pd^{2+} species. a.u., arbitrary units.

the calculated Rayleigh distributions for a random distribution over the host (Fig. 2a). Elemental mapping supports the uniform concentration of Pd over the carrier particle, and additional imaging on a standard microscope confirms the absence of nanoparticles (Supplementary Fig. 3). Consistently, no Pd–Pd bond was detected based on analysis of the X-ray absorption spectra; the two peaks centred at 1.07 and 1.55 Å confirm the coordination of palladium to nitrogen, and possibly to carbon, in the host.

The electronic properties of the Pd atoms incorporated in the ECN were probed by X-ray photoelectron spectroscopy (XPS). As expected, the Pd $3d_{5/2}$ spectra can be deconvoluted into two positively charged Pd species, tentatively assigned to Pd^{2+} at 336.5 eV and Pd^{4+} at 338.3 eV based on a comparison with database values, with a Pd^{2+}/Pd^{4+} ratio of 0.82 (Fig. 2d). The observed shifts can be caused partially by the isolated nature of the atoms as the Bader computed charge is 0.5 $|e^-|$ (ref. [19]). However, no bulk metallic signature appeared at 334.9 eV, in line with the absence of palladium nanoparticles in Pd-ECN evidenced by microscopy.

The performance of the Pd-ECN was initially evaluated in the continuous Suzuki coupling of bromobenzene with phenylboronic acid pinacol ester under optimized conditions (Supplementary Fig. 4), and benchmarked with the homogeneous and heterogeneous catalysts (Fig. 3). Pd-ECN proved to be a very effective catalyst that displayed a reaction rate of 0.57 $mmol_{product}\ min^{-1}\ g_{cat}^{-1}$ towards biphenyl (63% conversion, 90% selectivity and 56% purified yield), which outperformed all of the investigated homogeneous catalysts. Among these, only $Pd(PPh_3)_4$ demonstrated a similar performance (0.49 $mmol_{product}\ min^{-1}\ g_{cat}^{-1}$ (56% conversion, 88% selectivity and 41% purified yield)), whereas Pd(d*t*bpf)Cl_2 and $Pd(OAc)_2$ exhibited only minor rates to the desired product (0.03 and 0.06 $mmol_{product}\ min^{-1}\ g_{cat}^{-1}$, respectively). Comparatively, the grafted PdAc-MPES/SiO_2 catalyst showed a moderate performance (13% yield and 0.17 $mmol_{product}\ min^{-1}\ g_{cat}^{-1}$). In contrast, Pd/C (1 or 20 wt% Pd), which has been reported to efficiently catalyse the Ullmann homocoupling of aryl halides[20], was found to be inactive. Similarly, attempts to use Pd-Pb/$CaCO_3$ (5 wt% Pd and 3 wt% Pb), the dominant industrial catalyst for liquid-phase semi-hydrogenation reactions, were unsuccessful. Based on the total metal content, the turnover frequency (TOF) of Pd-ECN (549 h^{-1}) surpasses all the other catalysts by an order of magnitude (Fig. 3a). Impressively, in terms of TOF, Pd-ECN outperforms all the other catalysts reported for the reaction of aryl bromides with phenylboronic acid pinacol ester derivatives (Supplementary Table 1). A higher conversion could be achieved by increasing the catalyst amount without a significant loss of selectivity (Supplementary Fig. 5).

A major advantage of using Pd-ECN lies in its leaching resistance, which is clearly confirmed by the stable performance in continuous mode and corroborated by additional tests (Supplementary Fig. 6). This avoids complications of determining the nature of the active site faced in the batch mode[21]. Importantly, the tests evidence a constant rate towards biphenyl formation for over 13 h on stream with no variation in conversion or selectivity (Fig. 3b). Consistently, analysis of the used catalyst confirms the virtually identical amount (Fig. 3a), dispersion (Fig. 2b and Supplementary Fig. 2) and electronic properties (Fig. 2d) of Pd to the fresh Pd-ECN. This agrees with the high barrier (>2 eV) predicted for leaching ($Pd + 4PPh_3 \rightarrow Pd(PPh_3)_4$). Though it is not possible to evaluate the stability of the homogeneous catalyst equivalently, to shed light on this aspect the $Pd(PPh_3)_4$ was aged in a mixture with the reagents for different durations prior to reaction. Significant activity loss was observed after just two hours, and a characteristic colour change

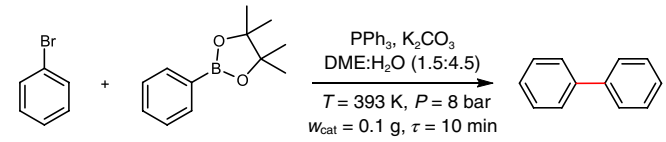

Sample	Pd (wt%)[a]	X (%)[b]	S (%)[b]	r (mmol min^{-1} g$_{cat}^{-1}$)[c]	TOF (h^{-1})[d]
Pd-ECN	0.66 (0.60)	63	90	0.57	549
$Pd(PPh_3)_4$	9.2	56	88	0.49	34
Pd(dtbpf)Cl_2	16.4	4	86	0.03	1.3
$Pd(OAc)_2$	47.4	8	79	0.06	0.9
PdAc-MPES/SiO_2	1.90 (0.60)	21	79	0.17	56
Pd-Pd/$CaCO_3$	5[e]	0	-	0	0
Pd/C	1[e]	0	-	0	0
Pd/C	20[e]	0	-	0	0

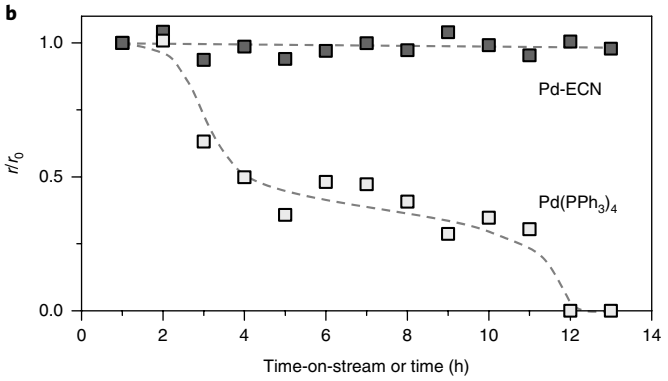

Fig. 3 | Evaluation of the C–C coupling performance. a, Reaction scheme and the performance in the continuous Suzuki coupling of bromobenzene with phenylboronic acid pinacol ester. The bond formed is indicated with a red line in the product. **b**, The relative rate (r/r_0) as a function of time-on-stream over Pd-ECN and ageing time over $Pd(PPh_3)_4$ catalysts. [a]ICP-OES (values in parentheses indicate the metal content of the used heterogeneous Pd catalysts after evaluation in the library of continuous-flow Suzuki couplings reported in Fig. 4). [b]Determined by high performance liquid chromatography (*X*, conversion; *S*, selectivity). [c]Rate of biphenyl formation per gram of catalyst. [d]Turnover frequency. [e]Nominal value. cat, catalyst.

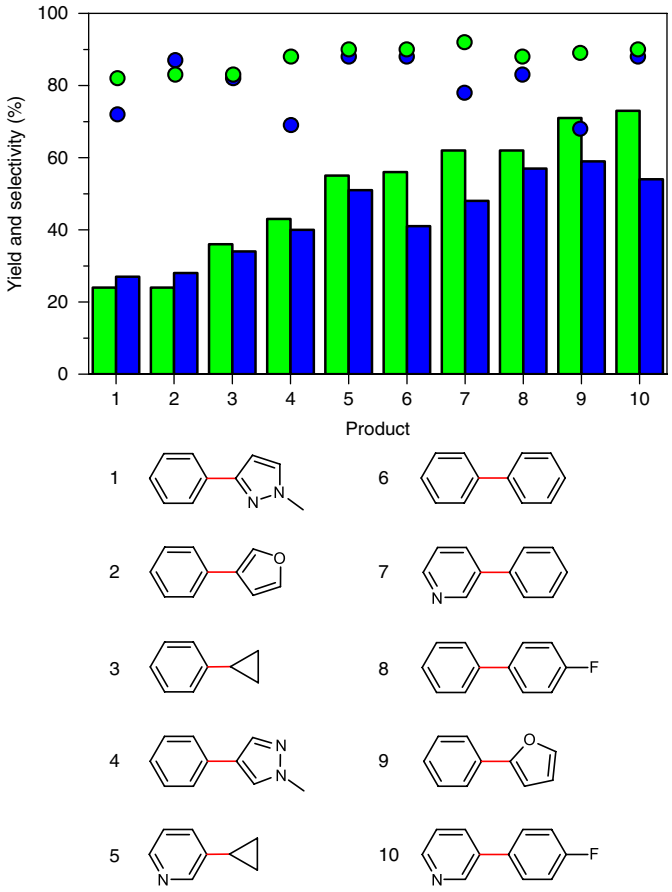

Fig. 4 | Comparative scope of Pd-ECN and $Pd(PPh_3)_4$ catalysts for Suzuki couplings. Yield (bars) and selectivity (circles) of the desired products (entries 1–10) over Pd-ECN (green) or $Pd(PPh_3)_4$ (blue). The newly formed C–C bonds are coloured red in the products. Reaction conditions as indicated in Fig. 3a. The specific substrates are detailed in Supplementary Table 6.

(from red to black) evidenced degradation of the catalyst via metal deposition, which highlights the challenge of using homogeneous catalysts for Suzuki couplings at a large scale. Comparatively, the heterogeneous PdAc-MPES/SiO_2 catalyst suffered from serious metal leaching that resulted in about a 70% loss of Pd (Fig. 3a and Supplementary Fig. 7).

The scope of Pd-ECN was further explored in the coupling of partner substrates, which included aryl, alkyl, alkenyl and heteroaromatic compounds (Fig. 4). The isolated Pd atoms afforded excellent purified yields to the desired products (24–73%), and outperformed (with a few exceptions) the homogeneous $Pd(PPh_3)_4$ counterparts. The fact that allcoupling reactions were conducted over the same cartridge also highlights the exceptional stability of this catalyst. Further insights into the performance were obtained by assessing the influence of the metal content (Supplementary Table 2). The rate of product formation showed an expected linear increase (from 0.22 to 0.57 $mmol_{product}$ min^{-1} g$_{cat}^{-1}$) with the palladium amount (from 0.25 to 0.66 wt%), but then decreased to 0.32 $mmol_{product}$ min^{-1} g$_{cat}^{-1}$ at 1.25 wt% Pd. A comparison on a metal basis revealed similar TOFs between 0.25 and 0.66 wt% Pd (558 and 549 h^{-1}, respectively), which confirms the equivalence of the additional sites in the latter sample. However, a significantly reduced TOF (163 h^{-1}) was observed on increasing the Pd content to 1.25 wt%. This observation suggests the formation of some clusters at this metal content, which further demonstrates the advantages of isolated single atoms over standard heterogeneous catalysts based on metal nanoparticles. To ascertain the impact of the host structure, an additional single-atom heterogeneous catalyst was prepared based on a mesoporous carbon nitride (Pd-MCN), which also displayed a high selectivity and stability, but was less active than Pd-ECN (Supplementary Table 3). The inferior performance is tentatively linked to the increased structural disorder exhibited by MCN compared to ECN (Supplementary Fig. 1). The results were also generalized by conducting reference batch experiments, the custom mode for Suzuki coupling reactions to date. A TOF of 1.9 h^{-1} (corresponding to a conversion of 7%) was obtained with 0.66 wt% Pd, which is comparable to other reported homogeneous catalysts in the same reaction (Supplementary Table 1, entries 4 and 5).

To understand the promising C–C coupling performance of Pd-ECN, we performed density functional theory (DFT) and

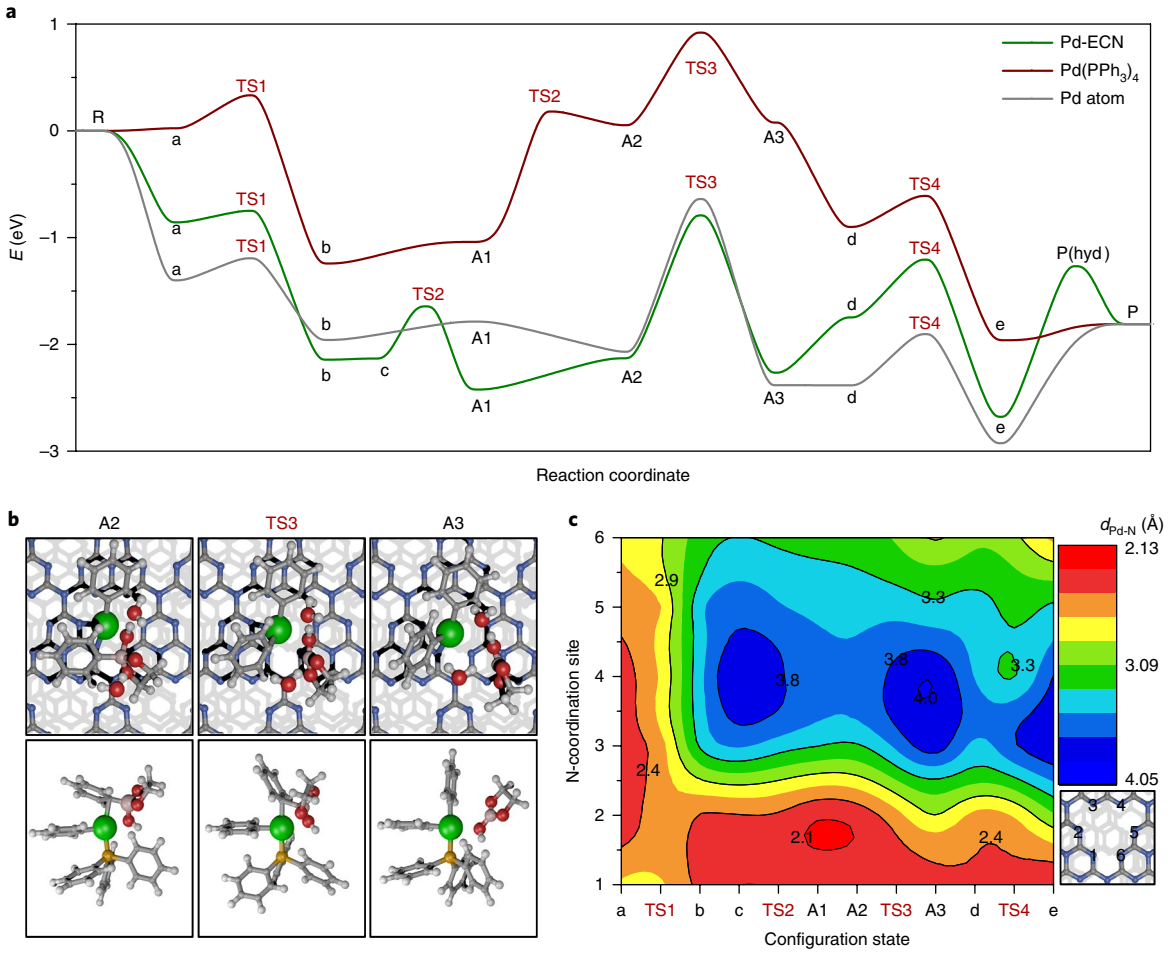

Fig. 5 | Reaction pathway of the Suzuki coupling. a, Energy profiles of the Suzuki coupling of bromobenzene with phenylboronic acid pinacol ester over Pd-ECN, $Pd(PPh_3)_4$ and an isolated Pd atom. The complete reaction paths are shown in Supplementary Fig. 9. TS1–TS4, transition states; a–e, starting and final states; A1–A3, transmetallation steps. R, reactants; P, products; hyd, hydrated. **b**, The transmetallation step (A2 → A3) for the indicated configuration of Pd-ECN (top) and $Pd(PPh_3)_4$ (bottom). Pd, green; C, grey; N, blue; H, white; O, red; B, pink. **c**, Contour plot of the interatomic Pd–N distances (*d*) for each N-coordination site (schematically identified in the bottom right) at each of the intermediate and transition states indicated in **a**. The corresponding values are reported in Supplementary Fig. 13.

molecular dynamics calculations. These focused on the ideal crystalline structure of graphitic carbon nitride as alternative binding sites that resulted in a lower adsorption affinity for the metal or were incompatible with the observed C/N ratio in the scaffold (Supplementary Fig. 8 and Supplementary Table 4). The Pd atoms were found to be slightly off centre from the sixfold N-coordination sites in the lattice due to the positively polarized N atoms and partially aromatic heptazine cores. Molecular dynamics simulations conducted at different temperatures show that, though the Pd atoms have some degree of freedom, they remain confined within a given cavity (Supplementary Video 1), which is consistent with the high stability of the catalyst. Interestingly, in agreement with the experimental XPS observations, two preferred positions are identified, one with the Pd atom located close to the surface plane and a second, favoured at higher temperatures, in which the metal sits between the two top planes. In the surface plane, the DFT-calculated XPS binding energies indicate a less-oxidized state, whereas a positive shift (by 2.5 eV) is evidenced in the subsurface pocket.

To search for the reaction path, we applied DFT (Fig. 5 and Supplementary Video 2). At the beginning of the reaction cycle, the coordination number of palladium to the lattice is close to six, and was thus normalized to this value (normalized coordination number, NCN). This structure molecularly adsorbs bromobenzene (state a in Fig. 5a) and presents a low barrier for activation (TS1, 0.11 eV); the relevant energies and the changes in Bader charges are presented in Supplementary Table 5. The reaction is exothermic by more than 1 eV, which leads to a configuration (state b in Fig. 5a) in which the Pd reduces its coordination to the lattice N sites to 3.2. This adaptive coordination appears in several steps and is crucial to the observed catalytic performance. Then, the adsorption of hydrated (two water molecules) potassium phenylboronate acid pinacol ester occurs (state c in Fig. 5a). This process is thermoneutral and the cation from the salt ends up in a nearest-neighbour empty cavity, which decreases the coordination number with the scaffold to NCN = 2.8. This configuration allows the displacement of Br^-, a step that presents a relatively small barrier (0.5 eV). The process is slightly exothermic as Pd recovers part of the coordination to the lattice (NCN = 3.3). The displacement of Br^- allows the coordination of phenylboronate pinacol ester, an intermediate that resembles the organometallic structure reported by Thomas and co-workers[22,23]. The subsequent transmetallation step occurs with a barrier of 1.3 eV and is rate determining in the reaction (Fig. 5b). This parallels the well-documented Pd^0/Pd^{2+} cycle reported in the traditional homogeneous catalysts and nanoparticulate systems, and thus a similar mechanism is expected. In contrast,

in the alternative Pd^{2+}/Pd^{4+} cycle the oxidative addition is rate limiting[24]. The transmetallation is almost thermoneutral and leads to intermediate A3, in which the Pd is again poorly coordinated to the matrix (NCN = 2.6). The boronic acid pinacol ester can then be eliminated from the surface (state d in Fig. 5a), which leads to an increase in NCN = 3.0. Finally, the C-C bond is formed through TS4 with a barrier of ~0.7 eV. This process is exothermic by about 1 eV, and in the bisphenyl adsorbed state the coordination of Pd remains low (NCN = 3.0). The elimination of the product to the gas phase is endothermic and restores the initial coordination of the Pd atom.

The overall picture closely follows the molecular mechanism (Supplementary Fig. 9) with just a few differences[25–28]. The $Pd(PPh_3)_4$ catalyst requires the elimination of two ligands to open the coordination sphere prior to reaction (reference state a in Fig. 5a) and a third one during the transmetallation step (TS3). As entropic contributions are not considered[29], the reaction profile for $Pd(PPh_3)_4$ is shifted towards higher energies, similar to the case of an isolated Pd atom in vacuum. In addition, varying the temperature has limited impact on the reaction profile (Supplementary Fig. 10). The lability of ligands in the homogeneous systems is essential, but also increases the propensity of metal aggregation, consistent with the rapid catalyst degradation observed for $Pd(PPh_3)_4$. Alternatively, if the ligand–metal interaction is too strong, then the organometallic catalyst is poorly active as activation implies ligand removal. In the ECN scaffolds, the two terms are modulated in a versatile way: (1) the N sites fulfil the function of the ligands in homogeneous systems that provide the electronic density required for the activation of phenylbromide and (2) the flexible lattice enables an almost continuously variable coordination pattern that adapts to the charge on palladium along the reaction coordinate, which gives rise to the high stability (Supplementary Fig. 11). Comparison of the variation in the Bader charge of Pd in Pd-ECN shows that this remains similar along the entire pathway in the range 0.4–0.7 $|e^-|$ (Supplementary Table 5). In contrast, significant changes are observed for the homogeneous catalyst during the oxidative addition (state a to state b from –0.26 to 0.25 $|e^-|$) and the reductive elimination (transmetallation step A3 to the products from 0.29 to –0.26 $|e^-|$). Though the formal oxidation state cannot be directly assigned, given the classical picture of formal oxidation states this can be mapped to the Pd^0/Pd^{2+} cycle. Further improvements in microscopy and spectroscopy techniques to enable operando monitoring will undoubtedly bring valuable further insights into the changes in the chemical environment and binding of the metal atom during the reaction cycle (Supplementary Discussion)[30].

In conclusion, a stable heterogeneous single-atom palladium catalyst based on exfoliated graphitic carbon nitride has been identified for Suzuki coupling. This material surpasses the performance of state-of-the-art homogeneous catalysts and conventional heterogeneous catalysts based on nanoparticles or grafted molecular complexes, without evidencing metal leaching or aggregation after the reaction. The enhanced properties could be explained at the molecular level, which reveals the pivotal role of the carbon nitride host, which, in addition to enabling an adaptive coordination of the palladium, participates in the adsorption, stabilization and activation of the substrates and intermediates. The possibility to mimic the beneficial functions of the ligands in metal complexes in an extended scaffold is advantageous as it avoids the risk of catalyst deactivation associated with their necessary lability. Given the range of possibilities to tailor the composition and framework structure of carbon nitride and related materials, the findings highlight the wide technological potential of single atoms stabilized in appropriate hosts to enable the heterogenization of challenging chemical processes, making the manufacture of fine chemicals and pharmaceuticals more sustainable.

Methods

Methods, including statements of data availability and any associated accession codes and references, are available at https://doi.org/10.1038/s41565-018-0167-2.

Received: 13 November 2017; Accepted: 14 May 2018;
Published online: 25 June 2018

References

1. Yin, L. & Liebscher, J. Carbon–carbon coupling reactions catalyzed by heterogeneous palladium catalysts. *Chem. Rev.* **107**, 133–173 (2007).
2. Molnár, Á. Efficient, selective, and recyclable palladium catalysts in carbon–carbon coupling reactions. *Chem. Rev.* **111**, 2251–2320 (2011).
3. Brown, D. G. & Boström, J. Analysis of past and present synthetic methodologies on medicinal chemistry: where have all the new reactions gone? *J. Med. Chem.* **59**, 4443–4458 (2016).
4. Yang, H., Han, X., Li, G. & Wang, Y. N-heterocyclic carbene palladium complex supported on ionic liquid-modified SBA-16: an efficient and highly recyclable catalyst for the Suzuki and Heck reactions. *Green. Chem.* **11**, 1184–1193 (2009).
5. Liu, J. Catalysis by supported single metal atoms. *ACS Catal.* **7**, 34–59 (2017).
6. Zhang, H., Liu, G., Shi, L. & Ye, J. Single-atom catalysts: emerging multifunctional materials in heterogeneous catalysis. *Adv. Energy Mater.* **8**, 1701343 (2018).
7. Zhu, C. et al. Single-atom electrocatalysts. *Angew. Chem. Int. Ed.* **56**, 13944–13960 (2017).
8. Gates, B. C., Flytzani-Stephanopoulos, M., Dixon, D. A. & Katz, A. Atomically dispersed supported metal catalysts: perspectives and suggestions for future research. *Catal. Sci. Technol.* **7**, 4259–4275 (2017).
9. Lucci, F. R. et al. Selective hydrogenation of 1,3-butadiene on platinum–copper alloys at the single-atom limit. *Nat. Commun.* **6**, 8550 (2015).
10. Kyriakou, G. et al. Isolated metal atom geometries as a strategy for selective heterogeneous hydrogenations. *Science* **335**, 1209–1212 (2012).
11. Qiao, B. et al. Single-atom catalysis of CO oxidation using Pt_1/FeO_x. *Nat. Chem.* **3**, 634–641 (2011).
12. Zhang, H. et al. Catalytically highly active top gold atom on palladium nanocluster. *Nat. Mater.* **11**, 49–52 (2012).
13. Yang, M. et al. A common single-site Pt(II)–$O(OH)_x$– species stabilized by sodium on 'active' and 'inert' supports catalyzes the water–gas shift reaction. *J. Am. Chem. Soc.* **137**, 3470–3473 (2015).
14. Vilé, G. et al. A stable single-site palladium catalyst for hydrogenations. *Angew. Chem. Int. Ed.* **54**, 11265–11269 (2015).
15. Kwak, J. H. et al. Coordinatively unsaturated Al^{3+} centers as binding sites for active catalyst phases of platinum on γ-Al_2O_3. *Science* **325**, 1670–1673 (2009).
16. Chen, Z. et al. Stabilization of single metal atoms on graphitic carbon nitride. *Adv. Funct. Mater.* **27**, 1605785 (2017).
17. Liu, P. et al. Photochemical route for synthesizing atomically dispersed palladium catalysts. *Science* **352**, 797–800 (2016).
18. Grundner, S. et al. Single-site trinuclear copper oxygen clusters in mordenite for selective conversion of methane to methanol. *Nat. Commun.* **6**, 7546 (2015).
19. Vorobyeva, E. et al. Tailoring the framework composition of carbon nitride to improve the catalytic efficiency of the stabilised palladium atoms. *J. Mater. Chem. A* **5**, 16393–16403 (2017).
20. Feiz, A., Bazgir, A., Balu, A. M. & Luque, R. Continuous flow room temperature reductive aqueous homo-coupling of aryl halides using supported Pd catalysts. *Sci. Rep.* **6**, 32719 (2016).
21. Zhang, X. et al. C-C coupling on single-atom-based heterogeneous catalyst. *J. Am. Chem. Soc.* **140**, 954–962 (2018).
22. Thomas, A. A., Wang, H., Zahrt, A. F. & Denmark, S. E. Structural, kinetic, and computational characterization of the elusive arylpalladium(II)boronate complexes in the Suzuki–Miyaura reaction. *J. Am. Chem. Soc.* **139**, 3805–3821 (2017).
23. Thomas, A. A. & Denmark, S. E. Pre-transmetalation intermediates in the Suzuki–Miyaura reaction revealed: the missing link. *Science* **352**, 329–332 (2016).
24. Sundermann, A., Uzan, O. & Martin, J. M. L. Computational study of a new Heck reaction mechanism catalyzed by palladium(II/IV) species. *Chem. Eur. J.* **7**, 1703–1711 (2001).
25. Xue, L. & Lin, Z. Theoretical aspects of palladium-catalysed carbon–carbon cross-coupling reactions. *Chem. Soc. Rev.* **39**, 1692–1705 (2010).
26. García-Melchor, M. et al. Computational perspective on Pd-catalyzed C–C cross-coupling reaction mechanisms. *Acc. Chem. Res.* **46**, 2626–2634 (2013).
27. Busch, M., Wodrich, M. D. & Corminboeuf, C. Linear scaling relationships and volcano plots in homogeneous catalysis—revisiting the Suzuki reaction. *Chem. Sci.* **6**, 6754–6761 (2015).
28. Ortuño, M. A., Lledós, A., Maseras, F. & Ujaque, G. The transmetalation process in Suzuki–Miyaura reactions: calculations indicate lower barrier via boronate intermediate. *ChemCatChem.* **6**, 3132–3138 (2014).

29. Ahlquist, M. S. G. & Norrby, P.-O. Dispersion and back-donation gives tetracoordinate [$Pd(PPh_3)_4$]. *Angew. Chem. Int. Ed.* **50**, 11794–11797 (2011).
30. Kalz, K. F. et al. Future challenges in heterogeneous catalysis: understanding catalysts under dynamic reaction conditions. *ChemCatChem.* **9**, 17–29 (2017).

Acknowledgements

We thank ETH Zurich, the Swiss National Science Foundation (Grant no. 200021-169679) and MINECO (CTQ2015-68770-R) for financial support. E.F. thanks MINECO La Caixa-Severo Ochoa for a predoctoral grant through Severo Ochoa Excellence Accreditation 2014-2018 (SEV-2013-0319). M.A.O. acknowledges the Juan de la Cierva-Incorporación postdoctoral program (IJCI-2016-29762). S.M.C. acknowledges support from the Henslow Research Fellowship at Girton College, Cambridge. P.A.M. acknowledges the EPSRC (Grant no. EP/R008779/1) for funding. We thank ScopeM at ETH Zurich for access to its facilities, BSC-RES for providing generous computational resources, Diamond Light Source for access and support in the use of the electron Physical Science Imaging Centre (EM16967), R. Hauert for XPS measurements, D. N. Johnstone for assistance in acquiring data at ePSIC. G.V. and S.R. thank T. Weller (Idorsia Pharmaceuticals Ltd.) for his constant support.

Author contributions

J. P.-R. conceived and coordinated all stages of this research. E.V. and Z.C. prepared and characterized the catalysts. G.V. and S.R. undertook the catalytic tests. E.F., M.A.O. and N.L. conducted the computational studies. S.M.C. and P.A.M. conducted the AC-STEM analysis. Z.C., E.V., S.M., G.V., E F., N.L. and J P.-R. co-wrote the manuscript in discussion with other co-authors.

Competing interests

The authors declare no competing interests.

Additional information

Reprints and permissions information is available at www.nature.com/reprints.

Correspondence and requests for materials should be addressed to J.P.

Publisher's note: Springer Nature remains neutral with regard to jurisdictional claims in published maps and institutional affiliations.

Methods

Catalyst preparation. A bulk graphitic carbon nitride material (BCN) was prepared by calcining dicyandiamide (10 g) at 823 K (2.3 K min^{-1} ramp rate) in a crucible for 4 h under a nitrogen flow (15 cm^3 min^{-1}). The ECN carrier was obtained via the thermal exfoliation of BCN (2 g) at 773 K (5 K min^{-1} ramp rate) for 5 h in static air. The mesoporous form (MCN) was prepared by calcining cyanamide with SiO_2 nanoparticles applied as the hard templates[16]. Palladium was introduced via microwave-irradiation-assisted deposition. The carrier (0.5 g) was first dispersed in H_2O (20 cm^3) under sonication for 1 h. Then, an aqueous solution of $Pd(NH_3)_4(NO_3)_2$ (5 wt% Pd, 0.05 cm^3) was added dropwise and stirred overnight. Afterwards, the resulting solution was placed in a microwave reactor (CEM Discover SP), with a cyclic program of 15 s irradiation and 3 min cooling with 20 repetitions using a power of 100 W. The resulting powder was collected by filtration, washed with distilled water and ethanol, and dried at 333 K overnight.

Catalyst characterization. Inductively coupled plasma–optical emission spectrometry (ICP–OES) was conducted using a Horiba Ultra 2 instrument equipped with a photomultiplier tube detector. The catalysts were dissolved in a piranha solution and left under sonication until the absence of visible solids. Powder X-ray diffraction was performed in a PANalytical X'Pert PRO-MPD diffractometer operated in the Bragg–Brentano geometry using Ni-filtered Cu Kα ($\lambda = 0.1541$ nm) radiation. Data were recorded in the range $2\theta = 5–70°$ with an angular step size of 0.05° and a counting time of 2 s per step. Argon sorption was measured at 77 K in a Micrometrics 3Flex instrument, after evacuation of the samples at 423 K for 10 h. The surface area was determined via the Brunauer–Emmett–Teller method. XPS was performed in a Physical Electronics Instruments Quantum 2000 spectrometer using monochromatic Al Kα radiation generated from an electron beam operated at 15 kV and 32.3 W. The spectra were collected under ultrahigh vacuum conditions (residual pressure = 5×10^{-8} Pa) at a pass energy of 46.95 eV. All the spectra were referenced to the C 1*s* peak at 284.8 eV. Thermogravimetric analysis was performed in a Mettler Toledo TGA/DSC 1 Star system in air (40 cm^3 min^{-1}), heating the sample from 298 K to 1,273 K at a rate of 5 K min^{-1}. Conventional STEM imaging and energy dispersive X-ray spectroscopy measurements were performed on a Talos F200X instrument operated at 200 kV and equipped with an FEI SuperX detector. AC-STEM was performed using an FEI Titan3 80-300 (Thermo Fisher Scientific) microscope operated at 300 kV and equipped with a high-brightness XFEG electron source and a CEOS aberration corrector for the probe-forming lenses. Additional AC-STEM performed at an accelerating voltage of 60 kV used an ARM300CF (JEOL) microscope equipped with a cold field emission electron source and a JEOL ETA corrector for the probe-forming lenses, located in the electron Physical Sciences Imaging Centre (ePSIC) at the Diamond Light Source. Diffuse reflectance infrared Fourier transform spectroscopy was performed using a Bruker Optics Vertex 70 spectrometer equipped with a high-temperature cell (Harrick) and an HgCdTe (MCT) detector. Spectra were recorded in the range 4,000–400 cm^{-1} at room temperature under an Ar flow by coaddition of 64 scans with a nominal resolution of 4 cm^{-1}. ^1H (proton-decoupled) NMR spectra were recorded at room temperature on a Bruker 500 MHz spectrometer equipped with a DCH cryoprobe, on dissolution of the homogeneous catalyst in $CHCl_3$. Chemical shift values are reported in parts per million downfield using the residual solvent signals ($CHCl_3$) as an internal reference. X-ray absorption spectroscopy was conducted at the X10DA (Super XAS) beamline of the Swiss Light Source. The polychromatic beam from the 2.9 Tesla superbend magnet was collimated using a Pt-coated mirror, monochromatized using a Si(311) channel cut monochromator, and focused to a spot size of 500 × 100 µm (horizontal × vertical) using a Pt-coated toroidal bent mirror. Data were acquired from pressed pellets at the Pd K edge in transmission mode, using two Ar-filled ionization chambers placed before and after the pellet. For the absolute energy calibration, a Pd foil was measured simultaneously between the second and a third ionization chambers. All 15 cm long ionization chambers were filled with an Ar/N_2 mixture. The resulting spectra were energy calibrated, background corrected and normalized at the height of the edge step using the Athena program from the IFEFFIT software suite[31]. Fourier transformations were performed from 3 to 12 $Å^{-1}$.

Catalyst testing. The continuous-flow Suzuki coupling reactions were conducted in a tubular or fixed-bed microreactor (Supplementary Fig. 6). For the homogeneously catalysed reactions, the aryl bromide (1 mmol), boronic ester (1.5 mmol), potassium carbonate (3 mmol), triphenylphosphine ligand (0.3 mmol) and catalyst (0.1 g ($Pd(PPh_3)_4$, $Pd(dtbpf)Cl_2$ or $Pd(OAc)_2$) were dissolved in a mixture of dimethoxyethane (DME) (1.5 cm^3) and water (4.5 cm^3), and the mixture was pumped at a flow rate of 0.02 cm^3 min^{-1} through a Hastelloy coil reactor of 10 cm^3 internal volume. In the stability test, these quantities were scaled up 20 times. Prior to the reaction, the purity of the investigated homogeneous catalysts was confirmed by ^1H NMR spectroscopy (Supplementary Fig. 12). In the case of heterogeneously catalysed reactions, the catalyst (0.1 g (Pd-ECN, PdAc-MPES/SiO_2, Pd-Pb/$CaCO_3$ or Pd/C) for the kinetic experiments and 0.3 g (Pd-ECN, PdAc-MPES/SiO_2, Pd-Pb/$CaCO_3$ or Pd/C) for the high-conversion experiments, with particle size between 0.2 and 0.4 mm) was packed in a quartz column reactor (0.66 cm internal diameter) and the mixture of the aryl bromide (1 mmol), boronic ester (1.5 mmol), potassium carbonate (3 mmol) and triphenylphosphine ligand was pumped through the column at a flow rate of 0.01–0.2 cm^3 min^{-1}. In both cases, the reaction was performed under the following conditions: temperature $T = 323–413$ K, pressure $P = 2–10$ bar and residence time $\tau = 1–15$ min. To confirm the absence of leaching, the product solution from the reaction over Pd-ECN was recirculated through a cartridge that contained inert silica particles, which revealed no additional transformation. Batch experiments were undertaken in quartz reactors approximately 12 cm^3 in diameter, into which the aryl bromide (1 mmol), boronic ester (1.5 mmol), potassium carbonate (3 mmol), triphenylphosphine ligand (0.3 mmol) and the homogeneous or heterogeneous catalyst (0.05 g) were charged. The solids were dissolved or dispersed in a mixture of DME (1.5 cm^3) and water (4.5 cm^3). The reaction was performed at the following conditions: temperature $T = 368$ K, pressure $P = 1$ bar and reaction time $t = 12$ h. For batch experiments, the heterogeneous catalyst was removed by filtration of the solution prior to analysis. The reaction aliquot was analysed as such. Liquid chromatography–mass spectrometry analyses were performed with an analytical Agilent G4220A pump coupled with a Thermo MSQ Plus mass spectrometer (electrospray ionization (ESI+)) and ELSD Sedere Sedex 90 on the Zorbax RRHD SB-Aq column from Agilent Technologies. HPLC analytical purifications were performed with a Waters Symmetry Shield RP18 column and an acetonitrile/water mobile phase.

DFT. DFT simulations were performed using the Vienna Ab initio Simulation Package code[32,33]. ECN systems were modelled as four-layer slabs and a 2 × 2 unit cell was used with a *k*-point sampling of 3 × 3 × 1. The slabs were separated by 16 Å of vacuum, employing a dipole correction. The functional used during the simulations was generated at the Perdew–Burke–Ernzerhof level of approximation[34]. The inner electrons were replaced by projector augmented waves[35]. The valence electrons included were 16 for Pd, 5 for N, 4 for C, 6 for O, 3 for B, 7 for Br and K, and a single electron for H. A plane wave basis set was used with a kinetic energy cut-off of 450 eV. The D3 approach was used to introduce the van der Waals contributions[36]. The transition states were located using the climbing image nudged elastic band algorithm[37]. The use of two explicit water molecules agrees with previous computational results[28]. The contribution of vibrational entropies did not modify the reaction profiles for Suzuki coupling reactions. Ab initio molecular dynamics was employed to address the temperature effects on the Pd-ECN system. Each run comprised 500 heating steps with $\Delta T = 100$ K, followed by 500 equilibration steps at a constant temperature. This cycle was repeated five times, from 0 to 500 K. The total simulation was 10 ps with a 2 fs step. The results are summarized in Supplementary Video 1. All the structures have been uploaded to the ioChem-BD[38] database and can be retrieved at https://doi.org/10.19061/iochem-bd-1-76.

Data availability. The data that support the plots within this paper and other findings of this study are available from the corresponding author upon reasonable request. The *xyz* coordinates for the computational chemistry results can be found at https://doi.org/10.19061/iochem-bd-1-76.

References

31. Ravel, B. & Newville, M. Athena, Artemis, Hephaestus: data analysis for X-ray absorption spectroscopy using IFEFFIT. *J. Synchrotron Radiat.* **12**, 537–541 (2005).
32. Kresse, G. & Furthmüller, J. Efficient iterative schemes for ab initio total-energy calculations using a plane-wave basis set. *Phys. Rev. B* **54**, 11169–11186 (1996).
33. Kresse, G. & Furthmüller, J. Efficiency of ab-initio total energy calculations for metals and semiconductors using a plane-wave basis set. *Comput. Mater. Sci.* **6**, 15–50 (1996).
34. Perdew, J. P. et al. Atoms, molecules, solids, and surfaces: applications of the generalized gradient approximation for exchange and correlation. *Phys. Rev. B* **46**, 6671–6687 (1992).
35. Kresse, G. & Joubert, D. From ultrasoft pseudopotentials to the projector augmented-wave method. *Phys. Rev. B* **59**, 1758–1775 (1999).
36. Grimme, S., Antony, J., Ehrlich, S. & Krieg, H. A consistent and accurate ab initio parametrization of density functional dispersion correction (DFT-D) for the 94 elements H–Pu. *J. Chem. Phys.* **132**, 154104 (2010).
37. Henkelman, G., Uberuaga, B. P. & Jónsson, H. A climbing image nudged elastic band method for finding saddle points and minimum energy paths. *J. Chem. Phys.* **113**, 9901–9904 (2000).
38. Álvarez-Moreno, M. et al. Managing the computational chemistry big data problem: the ioChem-BD platform. *J. Chem. Inf. Model.* **55**, 95–103 (2015).